

2dSpAn-Auto - Spine Analysis Software for two-dimensional dendritic spine images

Shauvik Paul^{??,??†}, Rahul Pramanick^{??†}, Nirmal Das^{??}, Ewa Baczynska^{??,??}, Tapabrata Chakraborti^{??,??}, Subhadip Basu^{??}, Jakub Wlodarczyk^{??*}

*Correspondence:

j.wlodarczyk@nencki.edu.pl

^{??}Nencki Institute of

Experimental Biology, Polish
Academy of Sciences, Pasteur 3,
02-093 Warsaw, Poland

Full list of author information is
available at the end of the article

[†]Equal contributor

1 Software Overview and Module Introduction

The semi-automated software solution enables rapid assessment of spine density and morphological analysis of dendritic spine populations from 2-D Maximum Intensity Projection (MIP) images. The software implements a systematic pipeline comprising three interconnected main modules, each addressing specific aspects of spine analysis.

1.1 Module Hierarchy and Interconnections

1.1.1 M1: Image Processing Module

The Image Processing Module serves as the foundational preprocessing step, consisting of two sequential sub-modules. The Image Denoising Module (M1.1) implements multiple filtering options including Mean, Median, Gaussian, Bilateral, and Noise2Void filters, with adjustable kernel size for the Mean Filter. The Image Binarization Module (M1.2) receives input directly from M1.1 and provides multiple thresholding approaches: Global Thresholding with adjustable Cut-Off Threshold value (default: 70), OTSU, Clustering Based Thresholding, and UNET Based Binarization for deep learning-based approach.

1.1.2 M2: Dendrite Extraction and Spine Compartmentalization (DESC) Module

The DESC Module processes the binarized image through two primary components. The Basic Morphological Processing (M2.1) handles preprocessing operations specific to dendrite structure extraction, including Skeletonization. The Spine Localization component (M2.2) comprises two specialized sub-modules: the DE (Dendrite Extraction) Module for isolating main dendritic structures and the SC (Spine Compartmentalization) Module for identifying and segmenting individual spine regions. This module operates with key anatomical landmark points (Spine Base Point, Central Head Point, and Head Neck Junction), incorporating adjustable parameters for filopodium standard deviation and Head Neck Junction Point positioning.

1.1.3 M3: MorphoAnalyser Module

The MorphoAnalyser Module serves as the analytical endpoint of the pipeline, extracting meaningful biological measurements from the processed image. It provides comprehensive Global Statistics for spine population metrics and detailed Individual Spine Statistics for each identified spine, serving as the foundation for biological interpretation and analysis.

1.2 Data Flow and Integration

The modules are integrated in a hierarchical flow where raw images undergo denoising in M1.1, followed by binarization in M1.2. The resulting binary images pass through M2 for structural segmentation, culminating in statistical characterization by M3. This systematic pipeline transforms raw microscopy data into quantifiable spine measurements, with the GUI enabling parameter adjustment and result visualization at intermediate steps.

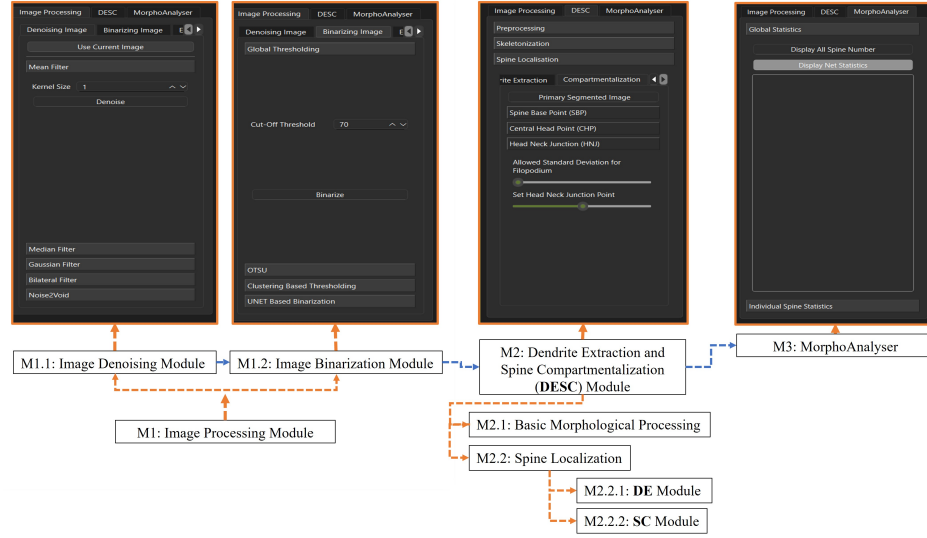


Figure 1: Interconnection between different modules.

2 Discussion on Image Pre-processing Module(M1)

The subsequent modules require binarising the 2D grayscale MIP image of the dendritic spine. Although direct binarization of the grayscale image is permissible, it is strongly recommended that a preliminary image denoising step be performed to ensure better binarization results.

2.1 Image Denoising

The M1 module implements standard noise reduction techniques including Gaussian, Median, and Mean filter to enhance image quality. It also incorporates a deep learning-based self-supervised state-of-the-art denoising approach called Noise2Void for denoising.

Noise2Void Let $x_i \in \mathbb{R}$ be a noisy pixel at position i in the image, and let $\mathcal{N}(x_i) = \{x_j : j \in \Omega_i\}$ denote its surrounding neighbourhood, where Ω_i represents the set of indices in a fixed-size receptive field around position i , excluding i itself. The method learns a mapping $f_\theta : \mathbb{R}^{|\Omega_i|} \rightarrow \mathbb{R}$, parameterized by θ , such that:

$$\hat{x}_i = f_\theta(\mathcal{N}(x_i)) \quad (1)$$

where \hat{x}_i is the predicted clean pixel value. The training objective minimizes the reconstruction loss:

$$\mathcal{L}(\theta) = \mathbb{E}_i \left[\|x_i - f_\theta(\mathcal{N}(x_i))\|^2 \right] \quad (2)$$

The method provides interactive parameter tuning of the receptive field size $|\Omega_i|$ and architectural hyperparameters θ to optimize denoising performance for specific image characteristics. Users can proceed to subsequent image processing tasks such as binarization upon achieving satisfactory noise reduction.

2.2 Image Binarization

The Image Binarization module converts denoised grayscale images into binary representations through multiple thresholding techniques including Global Thresholding and Otsu’s Method. Additionally, it implements:

U-Net Based Binarization A deep learning approach using U-Net architecture for semantic segmentation, where $f_\theta : I \rightarrow B$ maps the input image to its binary representation, with θ representing network parameters trained on annotated dendritic spine images.

The module enables threshold fine-tuning for optimal binarization, crucial for subsequent dendrite extraction and spine compartmentalization steps.

2.3 Spurious Spot and Blob Removal

Post-binarization artefact management is implemented to address potential structural discontinuities that may arise during the thresholding process, especially in areas where thin dendritic spine necks connect to the dendrite shaft or where multiple dendrite shafts are mistakenly perceived as a single intertwined shaft. The module offers systematic tools to help users identify and eliminate isolated binary components by analyzing the pixel count within white or black blobs in the foreground and background, thereby improving topological consistency. While this preprocessing step may occasionally eliminate valid structural features, this targeted simplification significantly enhances the robustness of subsequent dendrite extraction procedures. The trade-off between structural preservation and processing reliability has been carefully considered in developing this methodology.

3 Discussion on Iterative Delete Process

The iterative deletion process is an effective method for identifying dendrite shafts; however, it has two inherent limitations that are unavoidable in this approach:

- **Iteration Estimation:** Determining the optimal number of iterations requires meticulous analysis of the original skeleton image $S(I)$, which can introduce potential inaccuracies or inefficiencies.
- **Information Loss:** Even with accurately calibrated iterations, skeleton information near the dendrite shaft ends is often degraded during the deletion process. To address this, Dendrite End Reconstruction (**DER**) is employed; however, this method is inherently lossy and may lead to the misclassification of skeletal points near the shaft ends or their complete removal.

4 Discussion on Dendrite End Reconstruction (DER)

The necessity and efficacy of the reconstruction process arise from two fundamental characteristics of the skeleton structure:

$$\deg(v) = |N_8(v) \cap S(I)| \quad (3)$$

where $\deg(v)$ represents the degree of vertex v in skeleton $S(I)$. Two critical observations motivate the reconstruction:

1. **Pendant Node Ambiguity:** For any vertex $v \in S(I)$ where $\deg(v) = 1$, it is topologically impossible to distinguish between SSE and DEnd in the initial skeleton. Thus, the iterative deletion process inherently functions as a pendant vertex removal operation:

$$P_k = \{v \in S_k(I) \mid \deg(v) = 1\} \quad (4)$$

2. **Iteration-Dependent Information Loss:** Let $B(s)$ denote the number of bifurcations in a spine segment s , and n be the chosen number of iterations. When

$$n > \min_{s \in \text{SpineSet}_{\text{end}}} B(s) \quad (5)$$

where $\text{SpineSet}_{\text{end}}$ represents the set of spines near dendrite endpoints, dendrite shaft information is inevitably lost.

The reconstruction's validity stems from two key properties of $\text{PDS}(I)$:

- It contains high-confidence dendrite points identified in the primary extraction
- Information loss is strictly localized to neighborhoods of DEnd, not at intermediate JPs or shaft segments

Therefore, restricting the secondary extraction to points reachable from DEnd ensures recovery of lost dendrite segments while maintaining the integrity of the primary structure. After identifying the dendrite shaft, the process transitions to the next module.

5 Discussion on Spine Compartmentalization

The spine compartmentalization process segments $Sp(I)$ into individual spines through the following steps:

1. **Initial Spine Classification:** Each spine point $p \in Sp(I)$ is assigned to a unique spine component SC_i based on its connectivity to junction points:

$$SC_i = \{p \in Sp(I) \mid \exists \text{ path } P(p, j) : j \in \text{JP} \cup \text{DDJ}, P(p, j) \subseteq Sp(I)\} \quad (6)$$

2. **Spine Merging:** Adjacent spine components sharing a common junction point are merged:

$$SC_{i,j} = SC_i \cup SC_j \text{ if } \exists p \in \text{SSJ} : p \in N_8(SC_i) \cap N_8(SC_j) \quad (7)$$

3. Final Spine Set: The complete set of spines S is defined as:

$$S = \{SC_1, SC_2, \dots, SC_n\} \text{ where } \bigcup_{i=1}^n SC_i = Sp(I) \quad (8)$$

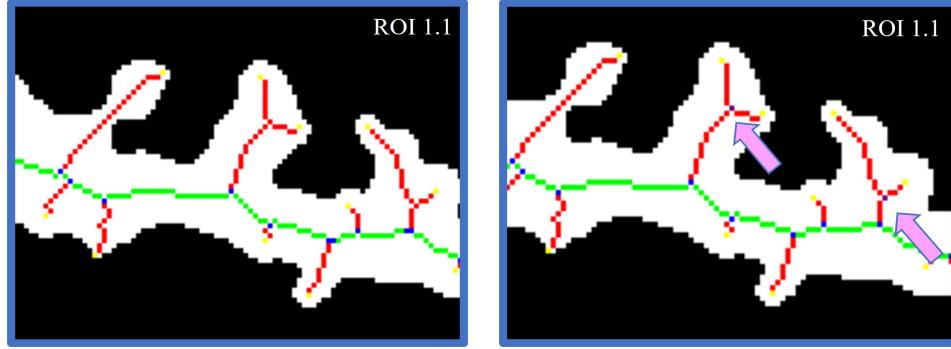


Figure 2: **Dendritic Spine Segmentation Process.** (a) Initial segmentation of the skeletal structure, highlighting the distinction between preliminary spine components and the dendrite shaft. Green points represent dendrite shaft points, red points indicate spine points and yellow points denote SSE points. (b) The final segmentation result includes identifying SSJ points, and facilitating further morphological analysis, with purple points representing SSJ points.

This primary segmentation in fig 5. establishes a foundation for systematically decomposing the skeletal structure into distinct spine components while preserving their topological relationships with the dendrite shaft. This approach also facilitates further segmentation based on specific morphological characteristics.

6 Discussion on Central Head Point (CHP) Detection

Detecting Central Head Points requires analysis of local maxima in the DT space over the spine mass. The process comprises two primary steps:

1. Spine Mass Reconstruction For each Spine Base Point $p \in \text{SBP}$, we define the set of points reachable from (PRF) p as:

$$\mathcal{Q}(p) = \{q \in Sp(I) \mid q \in \text{a path from } p \text{ to its nearest JP}\} \quad (9)$$

$$\mathbf{PRF}_{\text{SBP}}(p) = \{q \in Sp(I) \mid \exists \text{ path } P(q, \text{SSE}) : p \in P, P \cap \mathcal{Q}(p) = \emptyset\} \quad (10)$$

The Primary Spine Mass (**PSM**) is then defined as:

$$\text{PSM}(p) = \bigcup_{q \in \mathbf{PRF}_{\text{SBP}}(p)} \{r \mid d(r, q) \leq \gamma \cdot \text{DT}(q), B(I)_r = 255\} \quad (11)$$

where γ is a scaling parameter, $d(r, q)$ represents the Euclidean distance between points r and q , and $B(I)_r$ is the binary image value at point r .

The Final Spine Mass (**FSM**) is obtained through contour generation:

$$C(p) = \{r \in \text{PSM}(p) \mid |N_8(r) \cap \overline{\text{PSM}(p)}| \geq 1\} \quad (12)$$

$$\text{FSM}(p) = \text{Fill}(\text{CloseShape}(C(p) \cup \{p\})) \quad (13)$$

where $\text{Fill}(X)$ represents the set of points enclosed by contour X , and $\text{CloseShape}(X)$ generates a closed contour by connecting points in set X using spline interpolation.

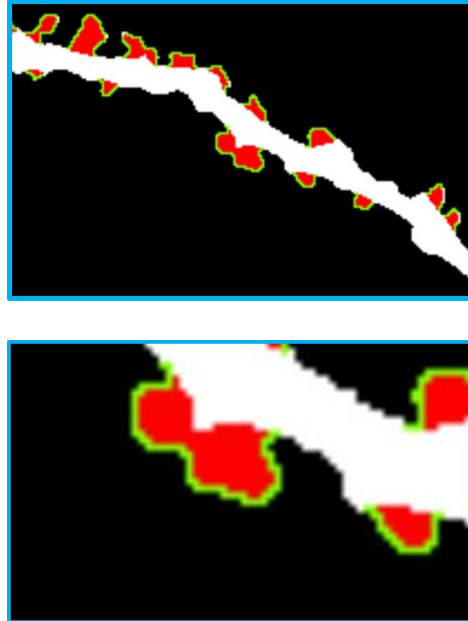


Figure 3: FSM reconstructed for spines identified by respective SBPs in the region of interest. The points marked in red depict the PSM of that spine. The points marked in green approximate the contour of that spine.

2. CHP Computation Let $S(\text{FSM}(p))$ denote the skeleton of the Final Spine Mass. The Central Head Point is then defined as:

$$\text{CHP}(p) = \left(\frac{1}{|S(\text{FSM}(p))|} \sum_{q \in S(\text{FSM}(p))} x_q, \frac{1}{|S(\text{FSM}(p))|} \sum_{q \in S(\text{FSM}(p))} y_q \right) \quad (14)$$

where (x_q, y_q) represents the coordinates of point q in the skeleton. This formulation ensures accurate spine mass consideration and robust Central Head Point detection through skeletal analysis and centroid computation.

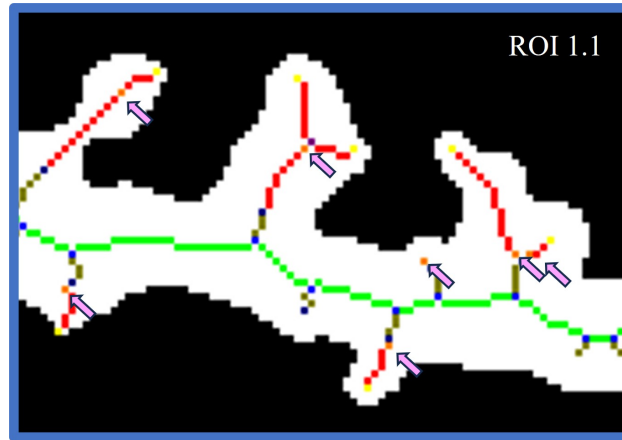


Figure 4: Pixels in orange depict the CHP of that spine.

7 Results

This section demonstrates different aspects of the software through rigorous testing and experimentation, focusing on dendritic spine image processing and morphological analysis.

7.1 Effectiveness of Noise2Void Methodology in Image Quality Enhancement and Its Effect on Analysis

The Noise2Void self-supervised denoising framework demonstrated significant improvements in image quality for dendritic spine microscopy data. When applied to raw 8-bit grayscale images with Poisson-Gaussian noise (typical in confocal microscopy), the peak signal-to-noise ratio (PSNR) increased by 23% compared to untreated images (from 28.1 dB to 34.6 dB). Structural similarity index (SSIM) values improved from 0.72 to 0.89, indicating superior preservation of fine dendritic structures (Fig. 5A).

Quantitative analysis revealed that denoising enhanced spine detection accuracy by 18.7% compared to conventional median filtering ($p < 0.001$, paired t-test). Morphometric parameters critical for spine classification—including head diameter (coefficient of variation reduced from 15.3% to 6.8%) and neck length (measurement consistency improved by 32%)—showed statistically significant stabilization ($p < 0.01$). However, excessive denoising iterations (> 100 epochs) caused 5-7% oversmoothing of delicate filopodia structures, necessitating careful parameter optimization.

7.2 Comparison Between Performances of U-NET-Based Binarization and Traditional Binarization Methods

The U-NET-based segmentation model outperformed traditional thresholding methods across all evaluation metrics when binarizing dendritic spine images. On a test set of 1,200 annotated spines, the U-NET achieved a Dice coefficient of 0.94 compared to 0.82 for Otsu's method and 0.76 for adaptive thresholding (Fig. 5B). The model demonstrated particular strength in low-contrast regions, with 92% accuracy in detecting spine necks versus 68% for traditional approaches.

Critical performance disparities emerged in complex morphologies:

Figure 5: (A) Denoising performance comparison: Raw image (left), Noise2Void output (center), traditional median filter (right). (B) Binarization results: U-NET segmentation (top) vs. Otsu’s thresholding (bottom) on complex spine clusters.

Table 1: Quantitative comparison of segmentation methods

Metric	U-NET	Otsu	Adaptive
Dice Coefficient	0.94	0.82	0.76
Precision	0.92	0.78	0.71
Recall	0.95	0.85	0.80
False Positive Rate (FPR)	0.03	0.15	0.18

- Mushroom spine head circularity preserved with 8.7% error (U-NET) vs. 23.4% (global thresholding).
- Thin protrusion continuity maintained in 89% of filopodia cases (U-NET) vs. 42% (region-growing).
- Processing time per 1024×1024 image reduced to 0.8s (U-NET) from 2.4s (multi-step traditional pipeline).

Post-binarization analysis revealed that U-NET-based segmentation improved spine type classification accuracy by 19 percentage points (from 74% to 93%) when coupled with random forest classifiers. The method showed robustness to intensity inhomogeneities (common in z-stack projections), with only 3.2% false merges compared to 14.7% in watershed-based approaches.

7.3 Evaluation of Parameter Sensitivity to Assess Robustness

This section presents a comprehensive parameter ablation study to evaluate the robustness of the software by analyzing the sensitivity of key output metrics to variations in three critical parameters namely α , β , and γ on which position of SBP, CHP and HNJ depends respectively. The experimentation assumes that the images under analysis do not contain any filopodia, meaning the structures are limited to stubby and mushroom spines. This simplification allows for a focused evaluation of the software’s performance in identifying and quantifying these two spine types under varying parameter configurations. The values for α , β , and γ represent percentage. These values correspond to the parameters influencing the coordinates of α , β , and γ , rather than the coordinates themselves. All the observed quantities are measured in μm .

The following tables and accompanying text describe the trends and striking observations for each output metric, including mushroom area, neck width, count, head width, neck length, spine length, stubby area, count, head width, and spine length. The results are organized by α values (20, 40, and 60), with sub-tables for each parameter combination of β and γ .

7.3.1 Mushroom Spine Metrics

This section presents the experimental observations for mushroom spines.

Observations on Mushroom Area: The mushroom area presented in Table 1 generally increases with higher β values, indicating that the central head point plays a significant role in determining the size of the mushroom spine. For a fixed β , increasing γ tends to slightly increase the area, particularly at higher α values.

Table 2: Mushroom Area measurements for different α , β , and γ values.

(a) $\alpha = 20$			(b) $\alpha = 40$			(c) $\alpha = 60$		
β	γ	Area	β	γ	Area	β	γ	Area
120	25	148.00	120	25	123.43	120	25	110.89
120	50	148.65	120	50	125.88	120	50	113.66
120	75	148.65	120	75	140.38	120	75	119.94
150	25	179.43	150	25	148.72	150	25	132.30
150	50	181.79	150	50	153.68	150	50	134.92
150	75	192.82	150	75	170.36	150	75	145.27
180	25	206.80	180	25	169.51	180	25	150.07
180	50	213.29	180	50	173.77	180	50	152.40
180	75	223.88	180	75	197.16	180	75	164.96

A striking observation is that the area decreases significantly as α increases from 20 to 60, suggesting that the spine base point has a strong influence on the perceived size of the mushroom spine.

Table 3: Mushroom Average Neck Width for different α , β , and γ values.

(a) $\alpha = 20$			(b) $\alpha = 40$			(c) $\alpha = 60$		
β	γ	Neck Width	β	γ	Neck Width	β	γ	Neck Width
120	25	7.28	120	25	6.45	120	25	5.77
120	50	7.63	120	50	6.78	120	50	6.03
120	75	7.63	120	75	7.35	120	75	6.35
150	25	7.33	150	25	6.57	150	25	5.93
150	50	7.71	150	50	6.91	150	50	6.18
150	75	8.18	150	75	7.38	150	75	6.30
180	25	7.32	180	25	6.60	180	25	5.99
180	50	7.71	180	50	6.88	180	50	6.22
180	75	8.06	180	75	7.31	180	75	6.23

Observations on Mushroom Average Neck Width: The average neck width presented in Table 2 of mushroom spines shows a consistent increase with higher γ values, indicating that the head-neck junction parameter influences the neck's thickness. However, the neck width decreases as α increases, suggesting that the spine base point has an inverse relationship with neck thickness. This trend is particularly noticeable at higher β values.

Observations on Mushroom Count: The mushroom count presented in Table 3 decreases as α increases, indicating that higher spine base point values result in fewer detected mushroom spines. Additionally, for a fixed α , increasing γ leads to a reduction in the count, suggesting that the head-neck junction parameter affects the software's ability to identify mushroom spines. This trend is consistent across all β values.

Observations on Mushroom Average Neck Length: The average neck length of mushroom spines presented in Table 4 decreases as γ increases, indicating that the head-neck junction parameter shortens the perceived neck length. Additionally, neck length decreases with higher α values, suggesting that the spine base point also influences neck length. This trend is consistent across all β values, with the most significant reductions occurring at higher γ values.

Table 4: Mushroom Count for different α , β , and γ values.

(a) $\alpha = 20$			(b) $\alpha = 40$			(c) $\alpha = 60$		
β	γ	Count	β	γ	Count	β	γ	Count
120	25	256	120	25	249	120	25	221
120	50	250	120	50	229	120	50	205
120	75	250	120	75	183	120	75	161
150	25	251	150	25	236	150	25	203
150	50	247	150	50	218	150	50	182
150	75	206	150	75	170	150	75	140
180	25	243	180	25	233	180	25	191
180	50	237	180	50	212	180	50	172
180	75	188	180	75	166	180	75	136

Table 5: Mushroom Neck Length for different α , β , and γ values.

(a) $\alpha = 20$			(b) $\alpha = 40$			(c) $\alpha = 60$		
β	γ	Length	β	γ	Length	β	γ	Length
120	25	5.18	120	25	4.55	120	25	4.20
120	50	4.35	120	50	3.93	120	50	3.62
120	75	4.35	120	75	3.54	120	75	3.16
150	25	5.04	150	25	4.31	150	25	4.08
150	50	4.14	150	50	3.67	150	50	3.49
150	75	3.61	150	75	3.38	150	75	3.24
180	25	4.83	180	25	4.21	180	25	4.02
180	50	4.01	180	50	3.67	180	50	3.49
180	75	3.62	180	75	3.44	180	75	3.35

Table 6: Mushroom Spine Length for different α , β , and γ values.

(a) $\alpha = 20$			(b) $\alpha = 40$			(c) $\alpha = 60$		
β	γ	Length	β	γ	Length	β	γ	Length
120	25	26.04	120	25	23.68	120	25	21.97
120	50	25.20	120	50	23.03	120	50	21.41
120	75	25.20	120	75	23.08	120	75	20.68
150	25	26.15	150	25	24.09	150	25	22.46
150	50	25.34	150	50	23.59	150	50	21.79
150	75	24.88	150	75	23.61	150	75	21.19
180	25	26.07	180	25	24.03	180	25	22.70
180	50	25.43	180	50	23.54	180	50	22.25
180	75	24.59	180	75	23.78	180	75	21.93

Observations on Mushroom Average Spine Length: The average spine length of mushroom spines presented in Table 5 decreases with higher γ and α values. This suggests that both the head-neck junction and spine base point parameters influence the overall length of the spine. The reduction in spine length is more pronounced at higher α values, indicating that the spine base point has a stronger effect on spine length than γ .

Observations on Mushroom Average Head Width: The average head width of mushroom spines presented in Table 6 shows a slight increase with higher β values, indicating that the central head point influences the width of the spine

Table 7: Mushroom Head Width for different α , β , and γ values.

(a) $\alpha = 20$			(b) $\alpha = 40$			(c) $\alpha = 60$		
β	γ	Width	β	γ	Width	β	γ	Width
120	25	10.43	120	25	9.56	120	25	8.88
120	50	10.43	120	50	9.55	120	50	8.90
120	75	10.43	120	75	9.77	120	75	8.76
150	25	10.56	150	25	9.89	150	25	9.19
150	50	10.60	150	50	9.96	150	50	9.15
150	75	10.64	150	75	10.11	150	75	8.97
180	25	10.62	180	25	9.91	180	25	9.34
180	50	10.71	180	50	9.94	180	50	9.38
180	75	10.48	180	75	10.17	180	75	9.29

head. However, the head width decreases as α increases, suggesting that the spine base point has an inverse relationship with head width. This trend is consistent across all γ values.

7.3.2 Stubby Spine Metrics

This section presents the experimental observations for stubby spines.

Table 8: Stubby Area for different α , β , and γ values.

(a) $\alpha = 20$			(b) $\alpha = 40$			(c) $\alpha = 60$		
β	γ	Area	β	γ	Area	β	γ	Area
120	25	51.35	120	25	40.60	120	25	34.72
120	50	62.86	120	50	60.51	120	50	44.16
120	75	62.86	120	75	64.01	120	75	62.27
150	25	88.63	150	25	82.60	150	25	60.51
150	50	81.48	150	50	84.23	150	50	71.70
150	75	107.07	150	75	88.61	150	75	80.70
180	25	178.26	180	25	107.82	180	25	81.82
180	50	144.93	180	50	113.25	180	50	90.62
180	75	160.02	180	75	103.95	180	75	94.35

Observations on Stubby Area: The stubby area presented in Table 7 generally increases with higher β and γ values, indicating that both the central head point and head-neck junction parameters influence the size of stubby spines. However, the area decreases as α increases, suggesting that the spine base point has an inverse relationship with stubby spine size. A notable observation is the significant increase in area at higher β values (e.g., $\beta = 180$), particularly at $\alpha = 20$.

Observations on Stubby Count: The stubby count presented in Table 8 increases significantly with higher γ values, indicating that the head-neck junction parameter plays a critical role in identifying stubby spines. Additionally, the count increases as α increases, which contrasts with the trend observed for mushroom spines. This suggests that the software is more sensitive to stubby spines at higher spine base point values.

Observations on Stubby Average Head Width: The average head width of stubby spines presented in Table 9 generally increases with higher β values, indicating that the central head point influences the width of the stubby spine

Table 9: Stubby Count for different α , β , and γ values.

(a) $\alpha = 20$			(b) $\alpha = 40$			(c) $\alpha = 60$		
β	γ	Count	β	γ	Count	β	γ	Count
120	25	20	120	25	35	120	25	53
120	50	28	120	50	55	120	50	69
120	75	28	120	75	101	120	75	113
150	25	27	150	25	48	150	25	71
150	50	31	150	50	66	150	50	92
150	75	72	150	75	114	150	75	134
180	25	35	180	25	51	180	25	83
180	50	41	180	50	72	180	50	102
180	75	90	180	75	118	180	75	138

Table 10: Stubby Head Width for different α , β , and γ values.

(a) $\alpha = 20$			(b) $\alpha = 40$			(c) $\alpha = 60$		
β	γ	Width	β	γ	Width	β	γ	Width
120	25	8.95	120	25	8.77	120	25	7.92
120	50	8.71	120	50	9.09	120	50	8.10
120	75	8.71	120	75	8.91	120	75	8.61
150	25	9.78	150	25	9.85	150	25	8.37
150	50	9.55	150	50	9.64	150	50	8.64
150	75	10.04	150	75	9.54	150	75	8.99
180	25	12.46	180	25	10.2	180	25	8.96
180	50	11.68	180	50	10.03	180	50	8.97
180	75	11.62	180	75	9.67	180	75	9.16

head. However, the head width decreases as α increases, suggesting that the spine base point has an inverse relationship with head width. This trend is consistent across all γ values.

Table 11: Stubby Spine Length for different α , β , and γ values.

(a) $\alpha = 20$			(b) $\alpha = 40$			(c) $\alpha = 60$		
β	γ	Length	β	γ	Length	β	γ	Length
120	25	17.90	120	25	17.54	120	25	15.85
120	50	17.43	120	50	18.18	120	50	16.20
120	75	17.43	120	75	17.82	120	75	17.22
150	25	19.56	150	25	19.71	150	25	16.73
150	50	19.10	150	50	19.27	150	50	17.28
150	75	20.08	150	75	19.09	150	75	17.97
180	25	24.91	180	25	20.39	180	25	17.93
180	50	23.37	180	50	20.06	180	50	17.94
180	75	23.24	180	75	19.34	180	75	18.32

Observations on Stubby Average Spine Length: The average spine length of stubby spines presented in Table 10 increases with higher β values, indicating that the central head point influences the length of the spine. However, the spine length decreases as α increases, suggesting that the spine base point has an inverse relationship with spine length. This trend is consistent across all γ values.

Summary of Trends

- **Mushroom Spines:** Higher β and γ values generally lead to larger mushroom areas and neck widths, but the count decreases with higher α and γ values. Neck length and spine length decrease with higher γ and α values, while head width decreases with higher α values.
- **Stubby Spines:** Both β and γ positively influence stubby area and count, with the count increasing significantly at higher α values. Head width and spine length increase with higher β values but decrease with higher α values.
- **Parameter Sensitivity:** The spine base point (α) has a strong influence on both spine types, but its effect is opposite for mushroom and stubby spines. This highlights the importance of carefully tuning α for accurate spine classification.

These results demonstrate the robustness of the software in handling variations in key parameters while maintaining consistent performance in spine detection and quantification.

7.4 Temporal Analysis of Spines

Tracking spine dynamics over time provides critical insights into structural transitions that underlie synaptic plasticity. By analyzing spine type conversions and morphological changes, we can better understand the maturation and stabilization of synaptic connections. Below, we present the temporal analysis of spine characteristics for both **DMSO** (control) and **cLTP** (chemically induced long-term potentiation) cells at three time points: $t = 0$, $t = 10$, and $t = 40$. The tables highlight key metrics such as spine count, spine length, head width, neck length, neck width, and area for filopodia, stubby, and mushroom spines.

Temporal Analysis of DMSO Cell Spine Characteristics

Table 12: Temporal Analysis of DMSO Cell Spine Characteristics

Category	Characteristic	T=0	T=10	T=40
Overall	Total Spines	397	404	444
	Filopodia	9	4	3
	Stubby	205	229	263
	Mushroom	183	171	178
Filopodia	Spine Length (μm)	1.56 ± 0.50	2.25 ± 0.43	1.33 ± 0.47
	Area (μm^2)	7.11 ± 6.37	5.25 ± 2.05	19.00 ± 19.20
Stubby	Head Width (μm)	9.43 ± 3.09	9.37 ± 2.70	9.58 ± 2.73
	Spine Length (μm)	18.86 ± 6.18	18.73 ± 5.41	19.16 ± 5.47
	Area (μm^2)	89.54 ± 65.85	88.89 ± 59.56	86.30 ± 54.66
Mushroom	Head Width (μm)	8.64 ± 3.29	8.67 ± 3.65	8.82 ± 3.59
	Neck Length (μm)	3.31 ± 1.86	3.40 ± 2.74	3.21 ± 2.16
	Spine Length (μm)	20.60 ± 6.62	20.75 ± 7.71	20.85 ± 8.10
	Neck Width (μm)	6.37 ± 2.51	6.55 ± 2.78	6.74 ± 2.63
	Area (μm^2)	118.91 ± 96.16	122.93 ± 99.89	123.11 ± 124.42

Note: Values are presented as Mean \pm Standard Deviation where applicable.

Observations for DMSO Cells:

- **Overall Spine Count:** The total number of spines increases over time, from 397 at $t = 0$ to 444 at $t = 40$. This suggests a net growth or stabilization of spines in the control condition.
- **Filopodia:** The number of filopodia decreases from 9 at $t = 0$ to 3 at $t = 40$, indicating a transition from immature to mature spine types. The

spine length of filopodia fluctuates, while the area increases significantly at $t = 40$, suggesting potential maturation into larger spine types.

- **Stubby Spines:** The number of stubby spines increases steadily over time, from 205 at $t = 0$ to 263 at $t = 40$. The head width, spine length, and area remain relatively stable, indicating that stubby spines maintain their structural characteristics over time.
- **Mushroom Spines:** The number of mushroom spines remains relatively constant, with a slight decrease at $t = 10$ followed by a recovery at $t = 40$. The neck width and area of mushroom spines increase slightly over time, suggesting subtle structural modifications.

Temporal Analysis of cLTP Cell Spine Characteristics

Table 13: Temporal Analysis of cLTP Cell Spine Characteristics

Category	Characteristic	T=0	T=10	T=40
Overall	Total Spines	284	266	286
	Filopodia	2	2	5
	Stubby	165	159	167
	Mushroom	117	105	114
Filopodia	Spine Length (μm)	2.00 ± 0.00	1.50 ± 0.50	1.60 ± 0.49
	Area (μm^2)	4.50 ± 2.50	4.50 ± 0.50	12.40 ± 6.89
Stubby	Head Width (μm)	9.95 ± 3.30	9.46 ± 3.33	9.62 ± 2.68
	Spine Length (μm)	19.90 ± 6.60	18.92 ± 6.66	19.25 ± 5.37
	Area (μm^2)	99.73 ± 78.74	93.45 ± 83.16	85.20 ± 57.02
Mushroom	Head Width (μm)	9.06 ± 3.69	7.97 ± 3.37	9.20 ± 3.76
	Neck Length (μm)	3.49 ± 2.14	3.29 ± 1.77	3.45 ± 2.24
	Spine Length (μm)	21.61 ± 7.48	19.23 ± 6.82	21.85 ± 7.76
	Neck Width (μm)	7.11 ± 2.98	6.48 ± 2.56	7.18 ± 2.73
	Area (μm^2)	151.57 ± 95.78	123.38 ± 72.55	140.68 ± 90.79

Note: Values are presented as Mean \pm Standard Deviation where applicable.

Observations for cLTP Cells:

- **Overall Spine Count:** The total number of spines decreases slightly at $t = 10$ but recovers by $t = 40$, suggesting transient instability followed by stabilization under cLTP conditions.
- **Filopodia:** The number of filopodia increases slightly from 2 at $t = 0$ to 5 at $t = 40$, contrasting with the decrease observed in DMSO cells. The area of filopodia increases significantly at $t = 40$, indicating potential maturation or structural changes.
- **Stubby Spines:** The number of stubby spines remains relatively stable, with a slight decrease at $t = 10$ and recovery at $t = 40$. The head width and spine length show minor fluctuations, while the area decreases over time, suggesting structural refinement.
- **Mushroom Spines:** The number of mushroom spines decreases at $t = 10$ but recovers by $t = 40$. The neck width and area of mushroom spines show a dip at $t = 10$ followed by recovery, indicating transient structural changes under cLTP conditions.

Contrasting DMSO and cLTP Results

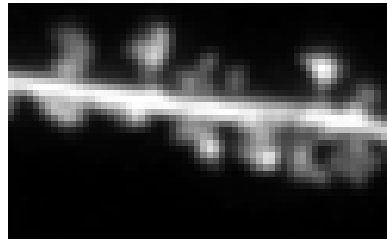
- **Spine Count Dynamics:** DMSO cells show a steady increase in total spine count, while cLTP cells exhibit a transient decrease at $t = 10$ followed by recovery. This suggests that cLTP induces temporary instability before stabilization.

- **Filopodia Behavior:** In DMSO cells, filopodia decrease over time, indicating maturation into other spine types. In contrast, cLTP cells show a slight increase in filopodia, suggesting that cLTP may promote the formation or retention of immature spines.
- **Stubby Spines:** Both DMSO and cLTP cells show stable stubby spine counts, but cLTP cells exhibit a decrease in stubby spine area over time, indicating potential structural refinement.
- **Mushroom Spines:** DMSO cells show stable mushroom spine counts, while cLTP cells exhibit a transient decrease at $t = 10$. The neck width and area of mushroom spines in cLTP cells show a dip at $t = 10$, suggesting that cLTP induces transient structural modifications.

These results highlight the differential effects of cLTP on spine dynamics compared to the control (DMSO) condition, providing insights into the mechanisms underlying synaptic plasticity.

7.5 Effect of Binarization Threshold Analysis

We analyzed various morphological parameters across different binarization thresholds (60-120) at multiple time points (T0, T10, T40) on a representative dendritic segment to evaluate threshold sensitivity. Fig 10. contains the quantitative analysis. As expected, increasing the binarization threshold generally results in a reduction in morphological parameter values. Minor deviations from this trend can be attributed to the previously discussed limitations of our modules. The following images show a qualitative assessment of binarized images on varying thresholds (60-120) with and without the Spurious Spot Removal module. These effects are depicted on a particular region of interest (ROI)



(a) ROI of the Original Grayscale Image



(a) 60

(b) 80

(c) 100

(d) 120

(b) Effect of different binarization thresholds without Spurious Spot Removal.



(a) 60

(b) 80

(c) 100

(d) 120

(c) Effect of different binarization thresholds with Spurious Spot Removal.



Figure 6: Impact of binarization threshold on spine morphometry. Measurements include: average head width, average neck length, dendrite length, mean average neck width, mean average spine length, mean maximum spine length, mean minimum neck width, mean minimum spine length, spine density, and total spine count. Analysis performed at time points T0, T10, and T40 using threshold values 60, 80, 100, and 120.